

Phonon-polariton excitations in photonic crystals

Kerwyn Casey Huang,* Peter Bienstman, John. D. Joannopoulos, and Keith A. Nelson

Center for Materials Science and Engineering, Massachusetts Institute of Technology, Cambridge, Massachusetts 02139, USA

Shanhui Fan

Department of Electrical Engineering, Stanford University, Stanford, California 94305, USA

(Received 25 October 2002; published 26 August 2003)

The incorporation of materials which exhibit transverse phonon-polariton excitations into a photonic crystal produces an intricate optical system possessing unique and varied photon phenomena. In particular, we demonstrate theoretically that such a system will exhibit both near-dispersionless bands with field localization in the polaritonic material and metalliclike bands with complete flux expulsion in an extremely small frequency interval around the characteristic phonon frequency. Moreover, when the fundamental resonances of the polaritonic rods overlap with the bands of a geometrically identical metallodielectric crystal, nearby states will couple to produce a band in which the localized field varies continuously between two distinct nodal patterns, in an exceedingly small frequency range. We also discuss the implications of losses on these phenomena and verify that our results can be realized experimentally.

DOI: 10.1103/PhysRevB.68.075209

PACS number(s): 71.36.+c, 42.70.Qs, 41.20.-q, 71.15.-m

I. INTRODUCTION

In recent years, the study of polar media which permit transverse phonon-polariton excitations has commanded great attention both experimentally¹ and theoretically² due to the unique and well-understood frequency-dependent dielectric function. In bulk polaritonic materials, there is a frequency range (the *polariton gap*) in which the propagation of electromagnetic (EM) waves is prohibited. Such a frequency range is generally called a photonic band gap (see Fig. 1). This photonic band gap (PBG) is unrelated to translational symmetry, unlike the PBG properties of crystals of constant dielectric materials, known as photonic crystals. Since the ground-breaking work of Yablonovitch,³ and John,⁴ the explosion of research into the design and fabrication of photonic crystals with complete PBGs (Ref. 5) has inspired a wealth of potential telecommunications applications, including waveguides, channel drop filters, and omnidirectional reflectors.^{6–8} We demonstrate how the substitution of polaritonic materials into photonic crystals introduces a whole range of exciting physical phenomena.

At a resonance between a transverse-optical phonon at frequency ω_T and a transverse EM wave, the phonon-photon coupling induces a radical change in the material's optical response. At low wave vectors, a simple model with dispersionless phonons yields the dielectric function⁹

$$\varepsilon(\omega) = \varepsilon_\infty \left(\frac{\omega^2 - \omega_L^2}{\omega^2 - \omega_T^2} \right), \quad (1)$$

where ε_∞ is the dielectric response at high frequency, and ω_L is related to ε_∞ and ω_T through the well-known Lyddane-Sachs-Teller relation $\omega_T \sqrt{\varepsilon(0)/\varepsilon_\infty}$. Clearly, the power of polaritonic materials lies in the opportunity to study the large epsilon and negative epsilon regimes using the same physical structure by merely choosing the frequency of light below ω_T or inside the polariton gap between ω_T and ω_L .

Various aspects of photonic band gaps and band structures of polaritonic photonic crystals (PPCs) have been previously studied using a diverse set of theoretical tools.^{10–15} Work by Sigalas *et al.*^{10,11} focused on determining the photonic band gaps in a two-dimensional (2D) photonic crystal slab composed of polar materials by analyzing the transmission coefficient as a function of frequency using the transfer-matrix method. To our knowledge, the first 2D PPC band structures were calculated by Zhang *et al.*¹² and followed by Kuzmiak, Maradudin, and McGurn.¹³ In both works, the authors identify as the major development the presence of flat, almost dispersionless bands below the phonon frequency ω_T .

Kuzmiak *et al.* postulated an explanation for these bands as coupling to the localized cavity modes of an isolated rod. We show that this proposition is indeed correct, by providing

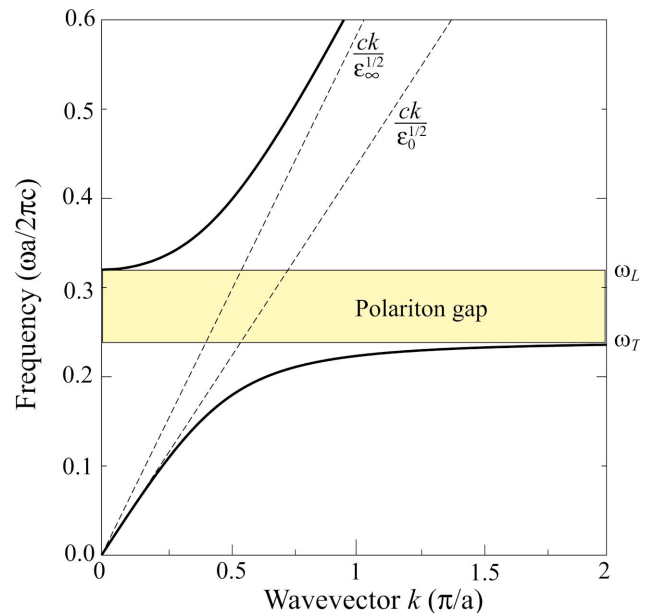


FIG. 1. (Color) Dispersion relation for a material with polariton dielectric function given by Eq. (1).

a fundamental model applicable in one, two, or three dimensions for photonic crystal properties in the large- ϵ regime that quantitatively explains the locations of the PPC bands below ω_T . In doing so, we demonstrate how the coupling can occur in totally different manners for the TE and TM modes depending on the location of ω_T relative to the bands of a metallodielectric crystal, with the polaritonic material replaced by a perfect metal. In some cases, the crystal will manifest an anticrossing behavior of the TE bands (\mathbf{H} out of plane) that has not been previously observed (due to the choice for $\omega_T a / 2\pi c$, where a is the PPC lattice spacing, of either 0.5 or 1.0 in the two other works^{12,13}).

In addition, we provide a description of the bands directly above ω_T , a metallic regime that has not been previously investigated. The presence of TE and/or TM bands which converge to ω_T is again regulated by the position of ω_T relative to the bands of the metallodielectric crystal. The situations in which bands exist arbitrarily close to ω_T both above and below lead to the introduction of a unique *flux expulsion* phenomenon, where light can be transferred completely in and out of the polaritonic material into the interstitial photonic crystal medium as ω sweeps across ω_T in an extremely small interval.

The paucity of previous PPC calculations is perhaps due to computational obstacles in traditional time-domain and plane-wave method (PWM) codes that crop up near the poles and zeros of ϵ at ω_T and ω_L , respectively. However, it is precisely these frequency ranges, where the materials divert from normal optical behavior, which we have found to be of particular interest. To overcome these difficulties, we employ a technique based on vectorial eigenmode expansion, discussed in Sec. II, which is ideally suited for frequency-dependent dielectrics and is accurate over an extremely large range of ϵ .

In Sec. III, we provide a comprehensive description of the band structures of 1D PPCs. We introduce our model for the flat bands below ω_T , and demonstrate the excellent agreement with our numerical results. We also characterize the bands inside the polariton gap at Γ , and demonstrate that for certain values of ω_T , ω_L , and ϵ_∞ , there can be a characteristic frequency at which the entire crystal becomes transparent. In addition, the simplicity of the 1D crystal allows us to provide an analytic solution for the wave vector of the bands at ω_L at which $\epsilon(\omega)$ goes to zero.

In Sec. IV, we adapt our model of the flat bands below ω_T to a 2D square lattice of polaritonic rods, and demonstrate the difference in behavior between TE and TM polarizations. The metallic bands directly above ω_T appear, and we explain how the band structure in these two regions can be simply tuned by varying ω_T , in particular, to exhibit flux expulsion. Finally, in Sec. V we discuss the effects of losses in the polaritonic material.

II. COMPUTATIONAL METHOD

To calculate the Bloch modes of a structure consisting of frequency-dependent materials, we use an approach based on vectorial eigenmode expansion.¹⁶ We identify a unit cell in the crystal oriented along a certain propagation direction, and

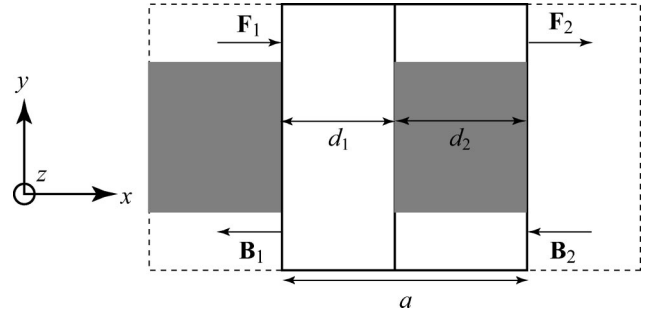


FIG. 2. Unit cell in a periodic structure marked by the solid outline. Note the axis convention which will be adhered to henceforth.

subsequently divide this cell into layers in which the index profile does not change in the propagation direction (see Fig. 2). In each of these layers, we expand the field in the local eigenmodes of that particular layer. The only approximation is the size of the eigenmode basis.

Using mode matching, we can eventually derive reflection and transmission matrices that completely describe the scattering behavior of the unit cell:

$$\mathbf{F}_2 = \mathbf{T}_{12} \cdot \mathbf{F}_1 + \mathbf{R}_{21} \cdot \mathbf{B}_2, \quad (2)$$

$$\mathbf{B}_1 = \mathbf{R}_{12} \cdot \mathbf{F}_1 + \mathbf{T}_{21} \cdot \mathbf{B}_2. \quad (3)$$

Here, \mathbf{F} and \mathbf{B} are column vectors containing the expansion coefficients of the forward and backward propagating fields, respectively, and \mathbf{T}_{12} , \mathbf{R}_{21} , etc. are explicit functions of frequency. We then impose Bloch boundary conditions

$$\mathbf{F}_2 = e^{-ika} \mathbf{F}_1, \quad (4)$$

$$\mathbf{B}_2 = e^{-ika} \mathbf{B}_1. \quad (5)$$

Equations (2) and (4) can be recast as a generalized eigenvalue problem, which can be solved for each frequency, where \mathbf{I} is the unit matrix and $q = e^{-ika}$:

$$\begin{bmatrix} \mathbf{T}_{12} & \mathbf{R}_{21} \\ 0 & \mathbf{I} \end{bmatrix} \begin{bmatrix} \mathbf{F}_1 \\ q\mathbf{B}_1 \end{bmatrix} = q \begin{bmatrix} \mathbf{I} & 0 \\ \mathbf{R}_{12} & \mathbf{T}_{21} \end{bmatrix} \begin{bmatrix} \mathbf{F}_1 \\ q\mathbf{B}_1 \end{bmatrix}.$$

In contrast to other approaches which compute the eigenvectors of the transfer matrix,^{17,18} no matrix inversions are required in our approach and therefore the method is numerically more stable. We also want to point out that in one dimension, this method is equivalent to the well-known transfer-matrix method (TMM).

Since the independent variable in these calculations is frequency rather than wave vector, it is trivial to account for material dispersion. Moreover, it is possible to increase the frequency resolution locally, an advantage over time-domain simulations where a frequency grid of increased resolution is implemented through a global increase in the number of time steps. This flexibility is exceedingly important for polaritonic materials, since there are rapid changes in the dielectric function over very small frequency intervals near ω_T . These

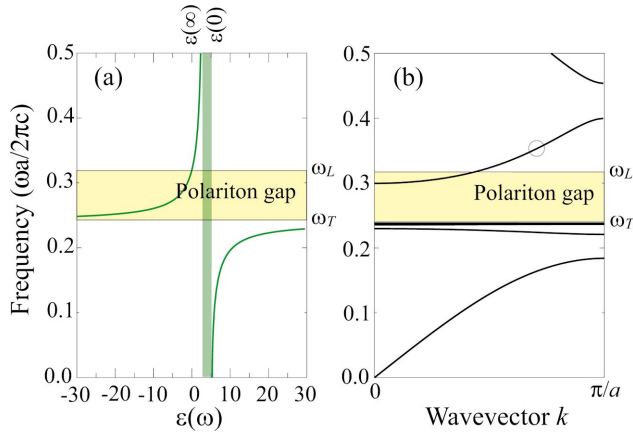


FIG. 3. (Color) (a) Polariton dielectric function of CsI with $\omega_T = 0.24$, $\omega_L = 0.32$, and $\epsilon_\infty = 3.0$. (b) Band structure of a 1D photonic crystal composed of CsI and air, with $d_1 = a/2$. Note the flat bands below ω_T , the penetration of the phononlike part of the band near ω_L into the polariton gap, and the transparency point (represented by the open circle) where $\epsilon = 1$ and the band intersects the line $\omega = ck$.

techniques were implemented in our generic photonic simulation tool CAMFR, which is freely available from <http://camfr.sourceforge.net>

A further restriction on time-domain and PWM calculations involving frequency-dependent dielectric functions is the necessity for a self-consistency loop when solving for the bands. In addition to the increased computational time, we have found the self-consistency step to introduce serious numerical instabilities in certain ranges, particularly where ϵ is very small. Kuzmiak *et al.*¹⁹ also mention the danger of missing zeros in the determinant of the matrix of expansion coefficients in the plane-wave expansion if the increment in frequency is too small. For the specific case of a polariton dielectric function, it is possible to recast the solutions to Maxwell's equations as a generalized eigenvalue equation using the plane-wave method to avoid the self-consistency loop,¹³ but for general frequency-dependent dielectric functions this simplification is impossible.

III. 1D POLARITONIC PHOTONIC CRYSTAL

We first examine the band structure of a 1D photonic crystal with propagation in the \hat{x} direction. The modes are TEM in this case, with both \mathbf{E} and \mathbf{H} parallel to the interface. For definiteness, we consider the polariton material CsI, with $\omega_T = 12 \times 10^{12}$ rad/s, $\omega_L = 16 \times 10^{12}$ rad/s, and $\epsilon_\infty = 3.0$.⁹ With a lattice constant of $a = 37 \mu\text{m}$, the polariton gap occurs between the normalized frequencies $\omega_T = 0.24$ and $\omega_L = 0.32$ (in units of $2\pi c/a$). For the most part, we will use air as the ambient material between polaritonic layers ($\epsilon_{\text{amb}} = 1$). The dielectric function and band structure are shown in Fig. 3.

There are three interesting features of Fig. 3(b) that are immediately apparent: (i) the flat bands below ω_T , (ii) the modes existing inside the polariton gap below ω_L , and (iii) the portion of the band around the frequency $\omega = 0.3533$

where $\epsilon = 1$ and the band intersects the line $\omega = ck$. One important question is whether our choice of polariton parameters $\{\omega_T, \omega_L, \epsilon_\infty\}$ holds any importance. In one dimension, the location of the polariton gap has little effect, but a different picture will emerge in two dimensions.

We study (i) by examining the modes of photonic crystals in the large index contrast limit. Our understanding of (ii) comes from an analytic solution of the wave vector at ω_L given by the TMM, and (iii) is a simple by-product of the transparency of the crystal at a particular frequency.

A. Large- n slab modes

As previously mentioned, other authors^{12,13} have observed the flat band phenomenon in PPCs below ω_T . However, what is missing is a theory to describe both qualitatively why the dispersion is so small, and quantitatively where these bands occur. We provide an answer to both of these issues in detail for a 1D PPC with a mind toward facilitating our future discussion in two dimensions. Directly below ω_T , the polariton material has a large index of refraction, and so in order to understand the flat bands in this frequency range, we initially ignore the frequency dependence of the material and consider a slab with fixed, large n . As $n \rightarrow \infty$, the reflectivity normal to an air interface may be shown to behave as

$$R = \left| \frac{n-1}{n+1} \right|^2 \rightarrow 1.$$

Hence, there are localized modes within the dielectric of the form $\varphi_m = \sin(\omega_m x)$, with frequencies $\omega_m = m\pi c/nd$. We note that these are of course only true localized modes in the limit $n \rightarrow \infty$; for finite n , the leakage of the fields into the air region allows for coupling between adjacent slabs and introduces frequency dispersion.

If we now assume a frequency-dependent dielectric function, the slab resonances also become frequency dependent. We can solve the equation $\hat{\omega}_m = \omega_m(\hat{\omega}_m) = m\pi c/d\sqrt{\epsilon(\hat{\omega}_m)}$ to obtain

$$\hat{\omega}_m^2 = \frac{1}{2} [\omega_L^2 + \Omega_m^2 - \sqrt{(\omega_L^2 + \Omega_m^2)^2 - 4\Omega_m^2 \omega_T^2}], \quad (6)$$

where $\Omega_m = m\pi c/d\sqrt{\epsilon_\infty}$.

In the limit of extremely localized fields, we expect the bands of the 1D polaritonic photonic crystal to follow a simple tight-binding model with a Hamiltonian

$$H\varphi_m = \hat{\omega}_m \varphi_m + T(\varphi_{m+1} + \varphi_{m-1}),$$

and bands of the form $\omega(k) = \hat{\omega}_m + T \cos(ka/\pi)$. The Hamiltonian has been linearized to obtain eigenvalues ω rather than the standard ω^2 by expanding in the small nearest-neighbor coupling integral T . Similar tight-binding models of photonic crystals have shown excellent agreement when the dielectric material has large ϵ .²⁰

In Table I, we compare the frequencies at $k = \pi/2a$ to $\hat{\omega}_m$ and find excellent agreement, to within 0.1%, for all $m > 1$. This clearly indicates that the localized mode model works beautifully and allows for the precise determination of not

TABLE I. Comparison of the band frequencies at $k = \pi/2a$ to $\hat{\omega}_m$ from Eq. (6) for a 1D crystal of CsI in air with $d_1 = d_2 = a/2$. In the last column is the value of ε at $\omega = \hat{\omega}_m$.

m	ω ($\pi/2a$)	$\hat{\omega}_m$	$\varepsilon(\hat{\omega}_m)$
2	0.2362	0.235 900	71.88
3	0.238 256	0.238 194	158.6
4	0.239 008	0.238 988	280.1
5	0.239 361	0.239 353	436.4
6	0.239 555	0.239 551	627.3
7	0.239 672	0.239 670	853.0
8	0.239 749	0.239 748	1113
9	0.239 801	0.239 801	1408
10	0.239 839	0.239 839	1738
11	0.239 867	0.239 867	2103

only the location of every band below ω_T but also, as we will examine more closely in two dimensions, the shape of the highly localized fields inside the polariton material.

B. Defectlike states in the polariton gap

We now turn our attention to the other side of the polariton gap. In Fig. 3(b), we see that in the range $\omega \in [0.2997, \omega_L]$ there are states inside the polariton gap, where $\varepsilon(\omega) < 0$. There is a simple interpretation of these modes. In the crystal, the slabs of air can be treated like defects in an otherwise homogeneous polariton material, drawing the states near $k=0$ around ω_L down into the gap. This is the opposite of the normal effect of air defects in a photonic crystal; the air becomes the higher index material when ω is near ω_L .

At $\omega = \omega_L$, the wave vector is given analytically by the TMM as

$$k(\omega_L) = \arccos \left[\cos \frac{\omega_L d_1}{c} - \frac{\omega_L d_2}{2} \sin \frac{\omega_L d_1}{c} \right]. \quad (7)$$

This wave vector is plotted in Fig. 4. Note that for $0.527 < \omega_L < 0.854$ there is a band in the polariton gap that extends throughout the Brillouin zone.

For the bands inside the polariton gap, we can characterize the decay rate of the field strength inside the polariton material of a mode of frequency ω_0 at $k=0$ by $\sqrt{|\varepsilon(\omega_0)|}$, which we plot in Fig. 5 as a function of ε_∞ for various values of ω_T and ω_L . We see that the decay rate increases with increasing ω_T or ω_L , and asymptotes as a function of ε_∞ .

C. Crystal transparency

The crystal becomes transparent to light at a frequency of $\omega_t = 0.3533$ in Fig. 3(b), where $\varepsilon = 1$ and the band intersects the line $\omega = ck$. In general, $\varepsilon(\omega) = \varepsilon_{\text{amb}}$ when

$$\omega^2 \equiv \omega_t^2 = \frac{1}{\varepsilon_\infty - \varepsilon_{\text{amb}}} (\varepsilon_\infty \omega_L^2 - \varepsilon_{\text{amb}} \omega_T^2) = \frac{\varepsilon_0 - \varepsilon_{\text{amb}}}{\varepsilon_\infty - \varepsilon_{\text{amb}}} \omega_T^2. \quad (8)$$

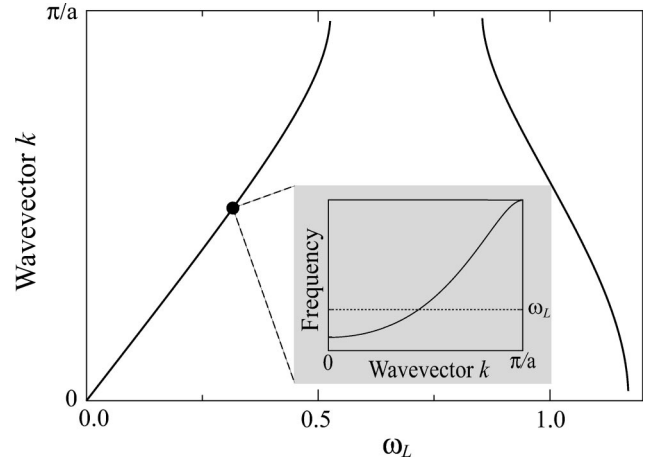


FIG. 4. The dependence of the wave vector k at $\omega = \omega_L$ on ω_L , according to Eq. (7). The black dot refers to the value of ω_L used to calculate the band shown in the inset intersecting $\omega_L = 0.32$ at $k = \pi/2a$ for a 1D crystal of CsI in air. Note that for $0.527 < \omega_L < 0.854$, there is a band entirely within the gap.

Note that when the slabs are in air, $\omega_t > \omega_L$. However, the point of transparency will be below ω_T when $\varepsilon_{\text{amb}} > \varepsilon_\infty$ and $\omega_T^2 > \omega_L^2 (\varepsilon_\infty / \varepsilon_{\text{amb}})$. This provides a unique tunability to a polaritonic system, since the transition to transparency can occur in a region of either rapidly or slowly varying index. In addition, note that there is no ω_t when $\varepsilon_\infty < \varepsilon_{\text{amb}} < \varepsilon_0$.

IV. 2D PHOTONIC CRYSTALS

We use our understanding of 1D crystals from the previous section to infer much of the relevant behavior in two dimensions. However, the existence of bands in a metallo-dielectric crystal will add rich, different phenomena and control possibilities that open the door for many exciting applications.

The band-structure calculations of Zhang *et al.*¹² exclusively use a polariton gap between $[0.5, 1.0]$, while those of Kuzmiak *et al.* use $[1, 1.08]$. However, we demonstrate that it is impossible to describe all of the complex elements of the band structures of 2D PPCs using a single choice of dielectric function parameters. The two-dimensional polaritonic photonic crystal that we examine consists of square rods of side $2r$ in air, with $2r/a = 0.25$, along the direction Γ to X .

A. Large- n cavities

We can understand the physics of a polaritonic crystal in two dimensions at frequencies below ω_T by first considering the modes of a square cavity in air with $k=0$ along the rod. As $n \rightarrow \infty$, the reflectivity goes to 1 at all angles away from Brewster's angle. To see how well this picture works for finite n , we compare the resonances of the square cavity to the metallic waveguide modes with frequencies

$$\omega_{lm} = \frac{\pi c}{2r\sqrt{\varepsilon}} (l^2 + m^2)^{1/2}, \quad (9)$$

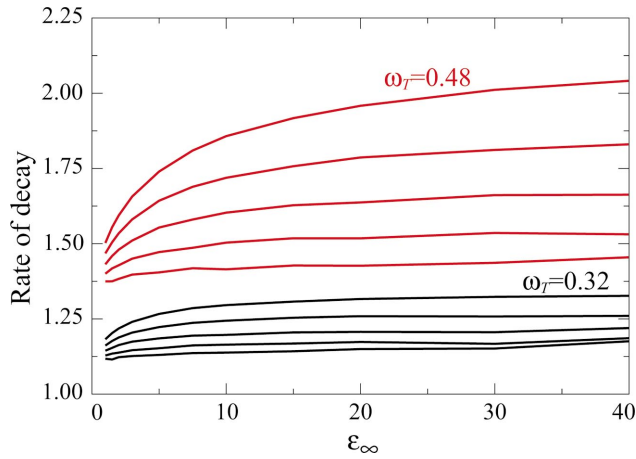


FIG. 5. (Color) The rate of decay of the field strength inside the polariton material of a mode of frequency ω_0 at $k=0$, given by $\sqrt{[\epsilon(\omega_0)]_{k=0}}$, as a function of ϵ_∞ . The black lines are for $\omega_T = 0.32$ ($2\pi c/a$) and red are for $\omega_T = 0.48$ ($2\pi c/a$). From bottom to top, the successive curves of each color are for ω_L from $\omega_T + 0.04$ ($2\pi c/a$) to $\omega_T + 0.2$ ($2\pi c/a$) in increments of 0.04 ($2\pi c/a$).

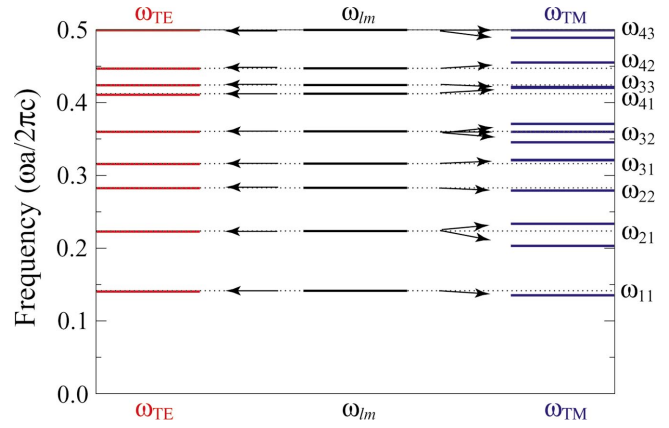


FIG. 6. (Color) Resonance frequencies of a square cavity with $n=20$ compared with the metallic waveguide frequencies ω_{lm} , shown as black horizontal lines in the center. TE modes are shown in red, TM in blue. The arrows indicate association between modes with fields of the same nodal structure.

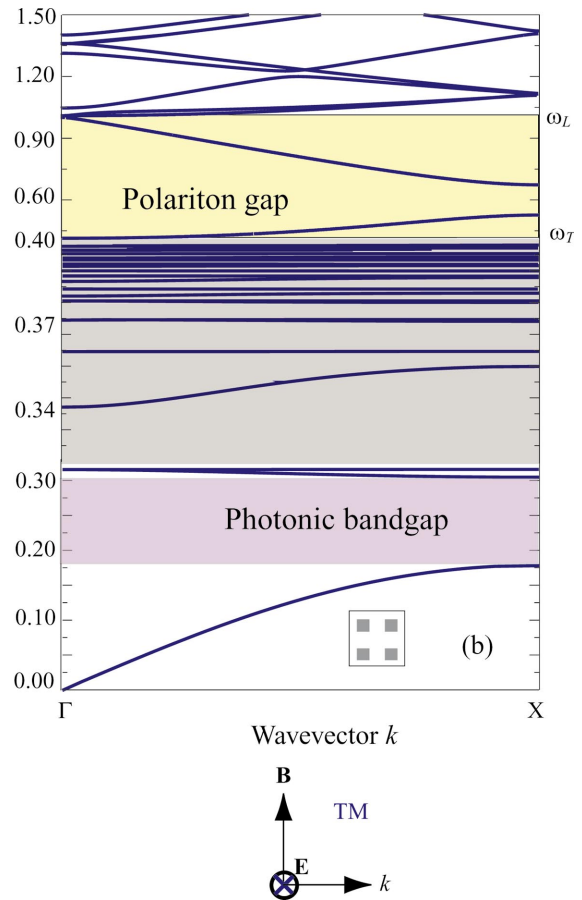
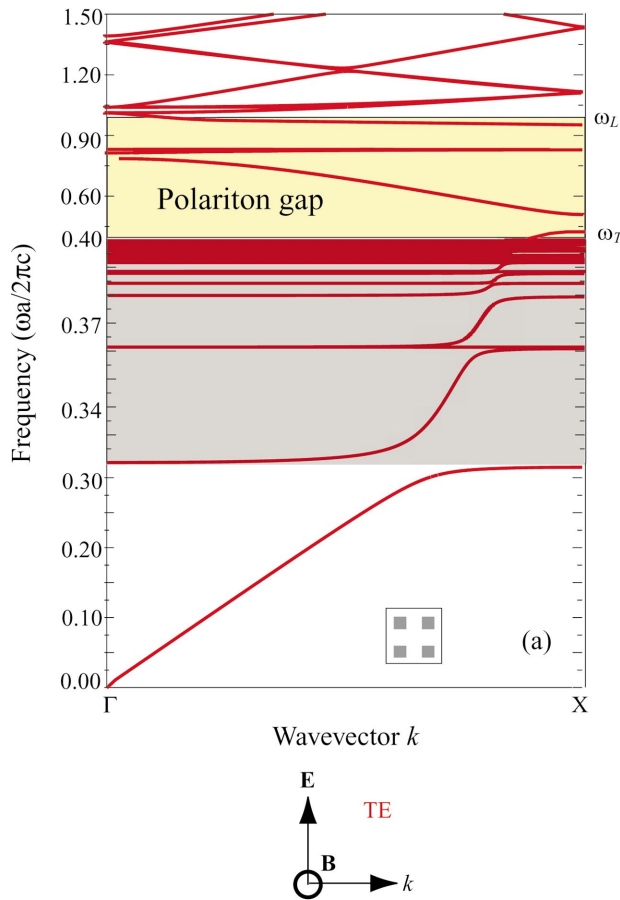


FIG. 7. (Color) Band structure of a 2D PPC of square TlCl rods in air with $2r/a=0.25$, $\omega_T=0.4$, $\omega_L=1.0$, and $\epsilon_\infty=5.1$. The TE bands are in red in (a), TM in blue in (b). Note the three different frequency spacings for the intervals $[0,0.32]$, $[0.32,0.4]$ (shaded in gray), and $[0.4,1.5]$. The primary photonic band gap in the TM modes is indicated by purple shading.

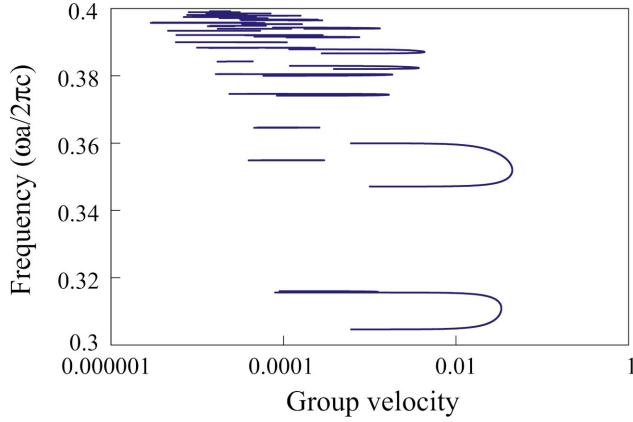


FIG. 8. (Color) Group velocity in units of $2c$ as a function of frequency of the TM bands displayed in Fig. 7 in a 2D TICl PPC.

where the modes with $l=0$ or $m=0$ are excluded from consideration since the fields should go to zero at the boundary. It is important to note, as in one dimension, that there are no true modes of the isolated rod with out-of-plane $k=0$, but rather pseudomodes that become exact only in the limit of infinite n . Keeping this in mind, we nevertheless refer to them as resonance modes, or resonance frequencies, since the true PPC states will retain the characteristics of these pseudomodes at finite n .

In Fig. 6, we plot the cavity resonance modes for a square rod with $n=20$ for both TE and TM polarizations and compare them to the model frequencies ω_{lm} . The correspondence was made by examining the field pattern inside the rod to determine the nodal pattern; the TE modes show slightly better agreement with the frequencies ω_{lm} .

We have used square rods because of the simple, analytic solution given in Eq. (9) for the metallic waveguide modes confined to the plane with zero out-of-plane wave-vector component. We infer that in a general 2D large- n photonic crystal, the band structure is governed primarily by the resonances of a single rod, whose frequencies are determined by the rod's geometry, where the periodicity of the crystal will only introduce slight dispersion.

B. 2D band structure

In this section, we use the insight gathered in Sec. IV A to understand the band structure of a 2D PPC in the high index region. In Fig. 7, we show the band structure for the polaritonic material TICl with $\omega_T = 12 \times 10^{12}$ rad/s, $\omega_L = 30 \times 10^{12}$ rad/s, and $\epsilon_\infty = 5.1$ (Ref. 9) (in normalized units, $\omega_T = 0.4$ and $\omega_L = 1$ for $a = 62.8 \mu\text{m}$).

The most striking feature is that the TE and TM bands exhibit very different behaviors. As expected, the TM bands closely resemble the 1D bands predicted by our simple tight-binding model since the \mathbf{E} field is continuous everywhere. We demonstrate the low amount of dispersion by plotting the group velocity as a function of ω for all of the TM bands below ω_T in Fig. 8.

However, the TE bands are roughly linear, except near particular frequencies (which we identify as resonances of a single rod) where they rapidly flatten. Let us examine this

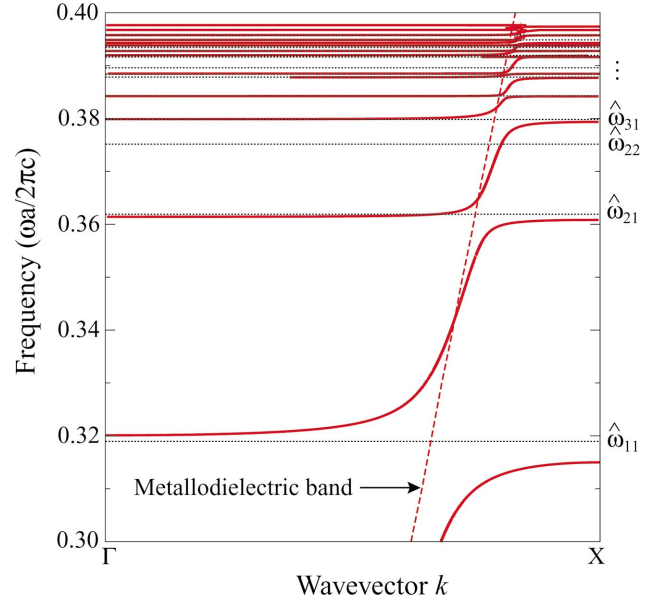


FIG. 9. (Color) Matching of the frequency-dependent metallic waveguide resonance frequencies $\hat{\omega}_{lm}$ from Eq. (10) to the 2D crystal band structure of TICl rods in air with $2r/a=0.25$. The resonance frequencies are displayed as horizontal black, dotted lines; the lowest TE band of the metallodielectric crystal is shown as a dashed red line.

behavior more closely. The frequency-dependent resonances solving $\hat{\omega}_{lm} = \pi c / 2r \sqrt{\epsilon(\hat{\omega}_{lm})}$ are

$$\hat{\omega}_{lm}^2 = \frac{1}{2} [\omega_L^2 + \Omega_{lm}^2 - \sqrt{(\omega_L^2 + \Omega_{lm}^2)^2 - 4\Omega_{lm}^2 \omega_T^2}], \quad (10)$$

where $\Omega_{lm} = \pi c (l^2 + m^2)^{1/2} / 2r \sqrt{\epsilon_\infty}$. In Fig. 9, these frequencies are overlaid upon the TE bands near ω_T , to show the close agreement. The largest gap at the band edges in the TICl crystal is relatively small (1.6%), occurring at the mid-gap frequency $\omega_{\text{mid}} = 0.3175$.

Why the difference between TE and TM modes? The answer lies in a comparison to the bands of a metallodielectric crystal with the same geometry of square metal rods, shown in Fig. 10. We point out one major difference between polarizations: the lowest TE band goes to zero frequency at Γ , lowest TM band has a frequency $\omega(\Gamma) = 0.409$. In addition, there is a gap at X in the TE bands between 0.458 and 0.517, while the lowest TM band has a frequency $\omega(X) = 0.546$.

It is clear from Fig. 9 that the lowest TE-polarized metallodielectric band increases in frequency from Γ to X in precisely the same fashion as the linear regions of the TE bands of the PPC. Thus, we interpret this observation as the anti-crossing interaction of the highly localized resonance modes of the polaritonic rods with the modes of the metallodielectric crystal (with the field completely removed from the rods), which is possible due to the small but finite leakage of the resonance modes out of the rods. In agreement with this simple characterization, the field near the band edges resembles the resonance mode of the rod closest in frequency.

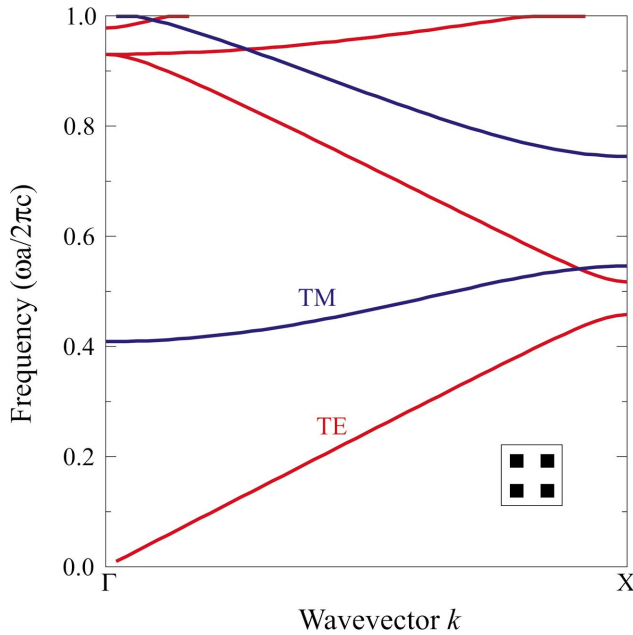


FIG. 10. (Color) Band structure of a 2D crystal of square, metallic rods (in black) in air with $2r/a=0.25$. TE bands are in red, TM in blue. Note the frequencies at the band edges of the first TE and TM bands.

The implications of this phenomenon on the importance of the location of the polariton gap are significant. There is a frequency cutoff $\omega_{\text{metal}}=0.458$, the maximum frequency of the lowest TE band of the metallodielectric crystal between Γ and X. Below ω_{metal} , all of the bands of the PPC are flat near Γ and X as a result of anticrossing between the metallodielectric TE mode and a particular rod resonance. Along a single band, the nodal surface of the field in the rod changes to match the two different resonance modes at Γ and X.

However, a drastic change in the band characterization occurs when $\omega_T > \omega_{\text{metal}}$. In Fig. 11, we plot the TE bands for an SiC crystal with $\omega_T=14.9 \times 10^{13}$ rad/s, $\omega_L=17.9 \times 10^{13}$ rad/s, and $\epsilon_\infty=6.7$ (Ref. 9) (in normalized frequency units, for $a=6.3 \mu\text{m}$, $\omega_T=0.5$, and $\omega_L=0.60067$). For this set of parameters, $\hat{\omega}_{11}=0.474$, and consequently we observe dramatically different behaviors from all of the TE bands in the TiCl crystal with $\omega_T=0.4$. Now all of the bands below ω_T , aside from the lowest, are very flat, much like the TM bands, representing a single resonance mode with slight dispersion resulting from interrod coupling of the weak fields outside the rods. In this case, the gaps are larger, reaching as high as 3.5% around $\omega_0=0.452$ in Fig. 11.

Returning to Fig. 9, we observe that there seems to be no interaction with the (2,2) resonance mode near $\hat{\omega}_{22}$. The fact that no anticrossing occurs for this and any of the modes (2l,2m) with even indices is a direct result of the common symmetry of these modes. From Fig. 12, it is clear that the H_z component of the lowest metallodielectric crystal TE mode has even symmetry in the plane with respect to reflection about the line parallel to the x axis crossing through the center of the cell. For any mode with even indices, H_z is odd, so the overlap integral is zero. This symmetry argument explains why none of the bands formed through anticrossing

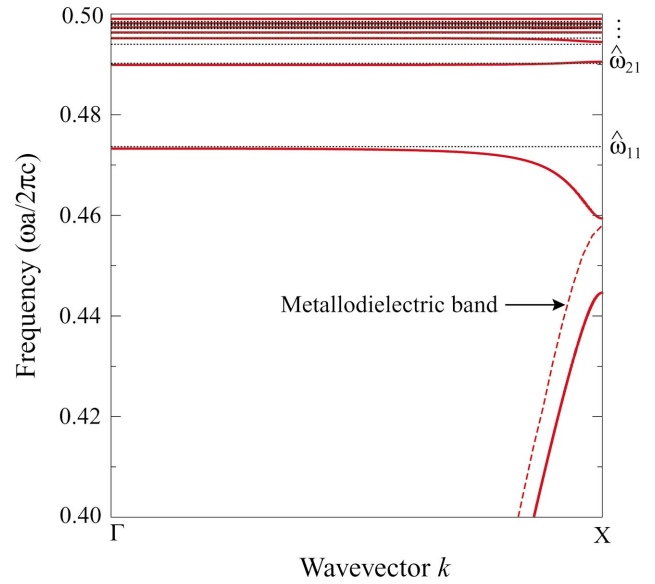


FIG. 11. (Color) Matching of the cavity modes $\hat{\omega}_{lm}$ from Eq. (10) to the 2D crystal band structure of SiC rods in air with $2r/a=0.25$. Note the distinctions from Fig. 9, due to the placement of ω_T above ω_{metal} .

will have field patterns resembling the (2l,2m) modes inside the rod, or resembling the one out of the two degenerate modes with frequency $\hat{\omega}_{2l,2m+1}$ with odd symmetry.

However, the question remains as to what happens to the modes of a single rod with odd symmetry in H_z once periodic boundary conditions are imposed. We expect that the same description that was used for the TM bands applies: a flat band should be formed near the frequency $\hat{\omega}_{lm}$ whose dispersion is a result only of weak interrod coupling between nearby cells. Due to the greater localization of the modes with TE polarization, the dispersion is extremely small. The fact that there is no band near $\hat{\omega}_{22}$ in Fig. 9 is simply a result of the frequency grid spacing being chosen too large. In Fig.

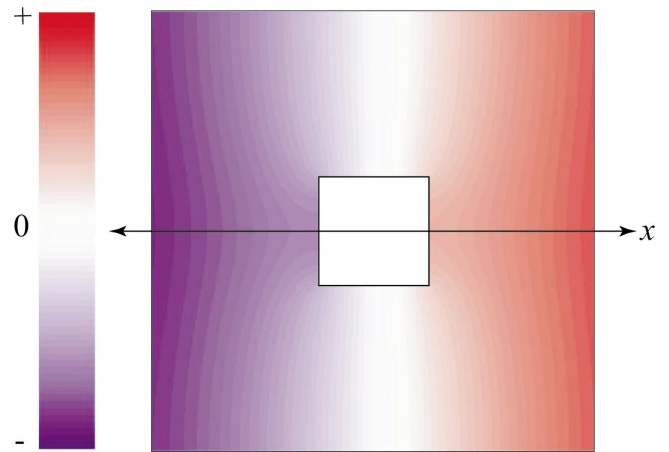


FIG. 12. (Color) The $\text{Re}[H_z]$ field pattern for the metallodielectric crystal TE mode at frequency $0.3 (2\pi c/a)$. Note the even symmetry in the plane with respect to reflection about the x axis. In this and all future field plots, blue indicates negative and red positive, with zero in white.

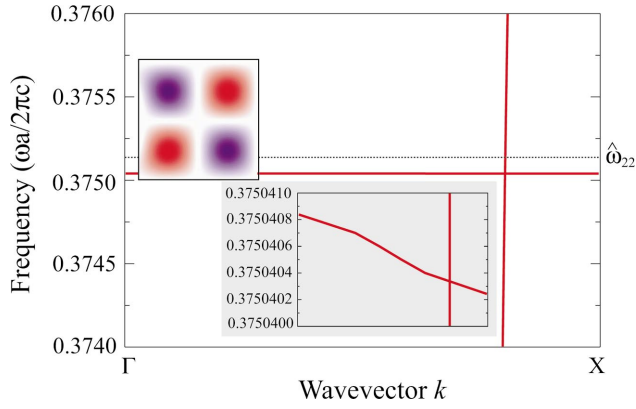


FIG. 13. (Color) The (2,2) localized resonance mode of the polariton rod, showing no anticrossing interaction. The H_z field pattern inside the rod is overlaid to show the odd symmetry with respect to reflection about the x axis. Note the frequency interval in the inset, demonstrating the extremely small bandwidth of 6×10^{-7} .

13, we observe that the band is in fact present and has a width on the order of 6×10^{-7} .

For the case of degenerate modes of frequency $\hat{\omega}_{2l,2m+1}$, we show in Fig. 14, using the (4,1) and (1,4) modes as an example, that the even-symmetry mode exhibits the anticrossing phenomenon, while there is a flat band corresponding to the mode of odd symmetry. Again, the bandwidth in this case is extremely small, on the order of 10^{-6} .

C. Node switching

There are several interesting metallic waveguide mode pairs connected by a single TE-polarized PPC band, such as $(l,m)=(4,1)$ and $(3,3)$, where the separation between the two frequencies $\hat{\omega}_{lm}$ in the PPC is extremely small [$0.0007 (2\pi c/a)$ for the TiCl crystal parameters in Sec. IV B]. Along this band, the nodal structure inside the rod is

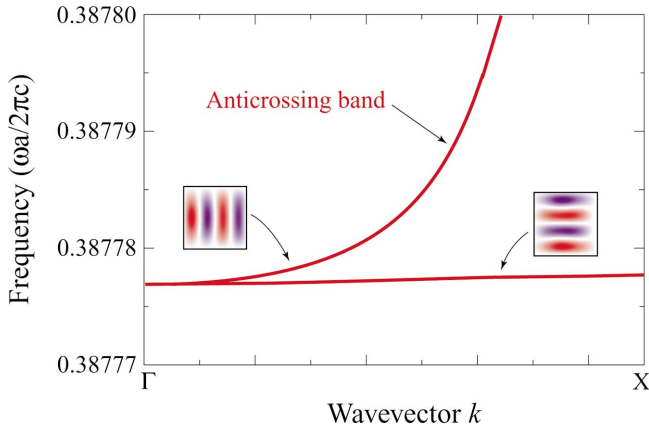


FIG. 14. (Color) The contrast between the interactions of the (4,1) and (1,4) modes with the lowest metallodielectric TE mode. The $\text{Re}[H_z]$ field patterns inside the polariton rod are overlaid. Note the anticrossing with the mode of even symmetry across the x axis, and the dispersionless band with bandwidth 8×10^{-7} for the mode of odd symmetry.

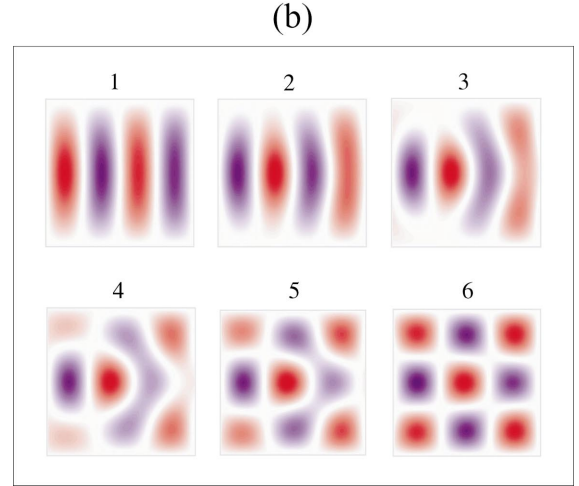
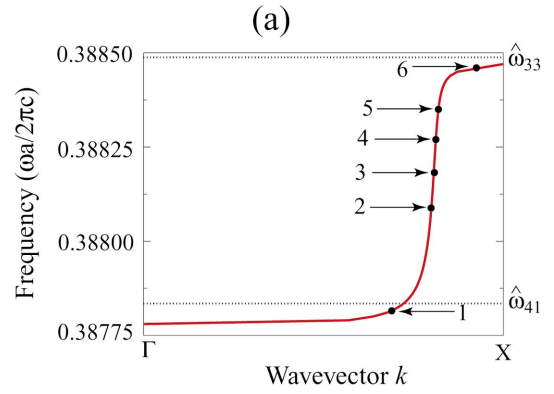


FIG. 15. (Color) Node switching. (a) The sixth TE band connecting the (4,1) cavity mode to the (3,3) cavity mode of a 2D PPC with square rods of TiCl, $2r/a=0.25$, with selected frequencies indicated by the numbered arrows. (b) The real part of H_z inside the rod at the frequencies indicated in (a) between 0.38779 and 0.38845.

forced to continuously change from one pattern to another, as shown in Fig. 15. This phenomenon provides an unprecedented capability for a state localized in the rod to change its coupling behavior over a very small frequency range. In terms of the practical impact of this phenomenon on potential applications, the fact that some of these mode pairs, e.g., (4,1) and (3,3) and (3,4) and (5,1), can be found at frequencies reasonably far away from the region near ω_T , where losses can become very large, bodes well for future research.

D. The metallic regime

We now switch gears, to the other side of the discontinuity of $\varepsilon(\omega)$ at ω_T . Above ω_T , $\varepsilon(\omega)$ is very negative, so we expect the polaritonic rods to behave as metals and expel nearly all of the field. Therefore, the possibility of finding bands in the region close to ω_T is governed by the existence of bands in the metallodielectric crystal in Fig. 10 at these frequencies. The positions of the gaps in both the TE- and TM-polarized bands mark exactly where polariton excitations are prohibited in the photonic crystal.

In Fig. 16(a), we plot the magnetic-field component H_z of the TE band at the frequency $\omega=0.44$, where $\varepsilon(\omega)=$

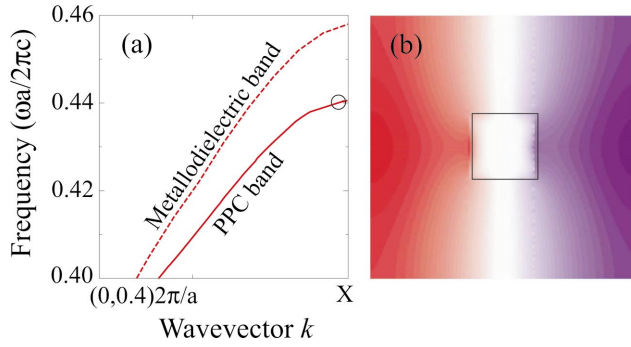


FIG. 16. (Color) Metallic behavior in the TE bands. (a) The first TE band above ω_T in a 2D TICl PPC is represented by the solid red line, with the corresponding portion of the lowest TE band in a metallodielectric crystal shown by a dashed red line. The open circle contains the portion of the PPC band at frequency $\omega=0.44$, for which the real part of the magnetic-field component H_z is plotted in a single supercell in (b), with the rod outline in black. The wave-vector axis begins not at Γ but at $0.8\pi/a$.

–65.2, for the same TICl PPC in Sec. IV B with $\omega_T=0.4$, $\omega_L=1.0$. We observe in Fig. 16(b) that there is no TM band at ω_T , as we would expect, since the lowest-frequency metallodielectric TM mode is at $\omega(\Gamma)=0.409$ (see Fig. 10).

In Fig. 17, we plot the electric-field component E_z at the frequency $\omega=0.523$ in a 2D square PPC of SiC rods. There is now no TE band at ω_T , since the phonon frequency is now within the TM gap [0.458,0.517]. Deviations from metallic behavior are slight for the entire band, even at $\omega=0.523$ near the band edge. Previous metallodielectric crystal band-structure calculations by Kuzmiak, Maradudin, and Pincemin,¹⁹ using the frequency-dependent dielectric function

$$\epsilon_{\text{metal}} = 1 - \frac{\omega_p^2}{\omega^2},$$

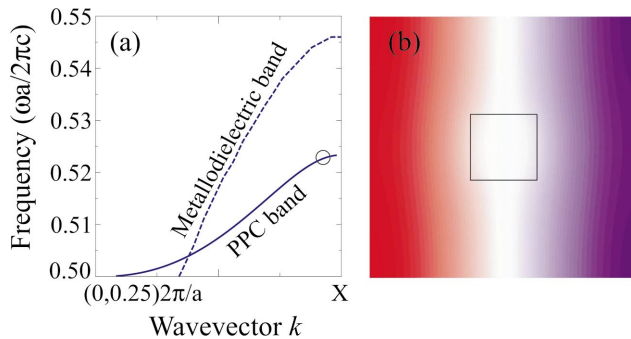


FIG. 17. (Color) (a) The first TM band above ω_T in a 2D SiC PPC shown by a solid blue line, with the corresponding portion of the lowest TM band in a metallodielectric crystal shown by a dashed blue line. The open circle contains the portion of the PPC band at frequency $\omega=0.523$, for which the real part of the electric-field component E_z is plotted in a single supercell in (b), with the rod outline in black. The wave-vector axis begins not at Γ but at $\pi/2a$.

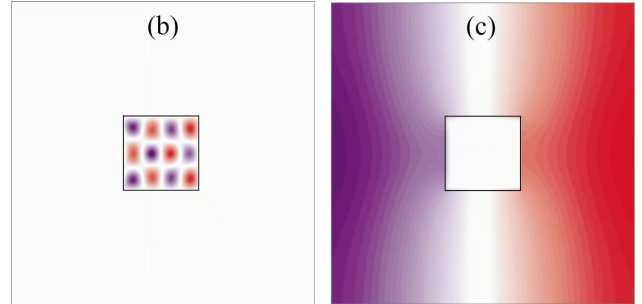
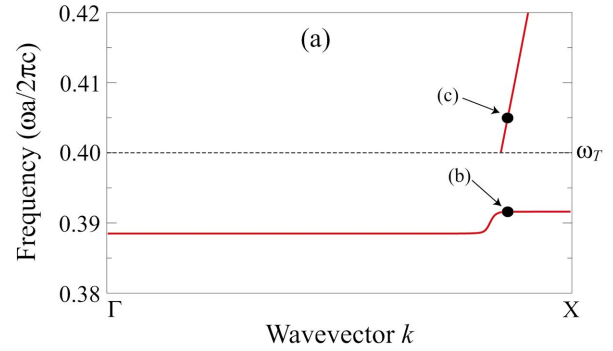


FIG. 18. (Color) Flux expulsion. (a) The band directly above ω_T and a flat band just below ω_T in a 2D PPC of TICl rods with $2r/a=0.25$. The Bloch states with $k=0.43$ ($2\pi/a$) at the frequencies $\omega=0.3916$ and $\omega=0.403$ are marked by arrows. (b) The field pattern of the real part of H_z at $\omega=0.3916$, where $\epsilon=649$. (c) The field pattern of the real part of H_z at $\omega=0.403$, where $\epsilon=-1773$. Note the extreme contrast between the localization of the field inside the rod in (b) and the complete flux expulsion in (c).

where ω_p is the plasmon frequency of the metal, have displayed similar behavior to that in Fig. 10 for frequencies below ω_p where $|\epsilon|$ is less than around 10, thus we are clearly well within the regime considered as metallic at $\omega=0.523$ since $\epsilon(\omega)=-24$.

These observations lead us to the introduction of the phenomenon of flux expulsion in PPCs, where small changes in ω near the interface between the metallic and dielectric photonic band-gap regimes can induce enormous variations in the topology of the field pattern. We demonstrate this phenomenon in Fig. 18. Using other geometries and/or other materials to surround the polaritonic medium (in particular, nonlinear materials), this tool should be extremely useful as a switch to shift light in and out of different physical regions of the crystal. In the following section, we examine more closely the effect of losses, and we find that for some polaritonic media, losses are restricted to a sufficiently small area around ω_T so that practical utilization of flux expulsion should be possible.

E. Other phenomena

We have chosen to focus on the large- n and metallic limits, because the physics in two dimensions versus one dimension occurs in these frequency ranges. However, the other two phenomena mentioned in Sec. III are still relevant: the transparency condition is unchanged, and there are bands

either close to or intersecting ω_L . In particular, although no analytic solution is known to exist for the wave vector at ω_L , we find that $k(\omega_L)$ is independent of ω_T , as was the case in one dimension.

V. LOSSES

In Secs. III and IV, we provided a comprehensive analysis of the band structures of photonic crystals in one and two dimensions composed of lossless polariton materials with a wide range of phonon frequencies and dielectric limits. The well-known model to correct for losses is the dielectric function

$$\epsilon(\omega) = \epsilon_\infty \left(1 + \frac{\omega_L^2 - \omega_T^2}{\omega_T^2 - \omega^2 - i\omega\Gamma} \right), \quad (11)$$

where the magnitude of the losses is represented by Γ . Sigalas *et al.* implemented Eq. (11) in their transmission calculations.¹¹ Shown in Fig. 19 are the real and imaginary parts of the dielectric function for LiTaO₃, using the parameters given by Schall *et al.*²¹ $\omega_T = 26.7 \times 10^{12}$ rad/s, $\omega_L = 46.9 \times 10^{12}$ rad/s, $\Gamma = 0.94 \times 10^{12}$ rad/s, and $\epsilon_\infty = 13.4$ along the ordinary axis of the atomic crystal.

Although losses will clearly become important near ω_T , at frequencies separated from ω_T by more than Γ the dielectric function is mostly unchanged and the effects of losses should be minimal. For the LiTaO₃ parameters given above, with a lattice constant of $a = 25.6 \mu\text{m}$, the second TE band of the lossless crystal will exhibit a transition from the $\hat{\omega}_{11} = 0.293 (2\pi c/a)$ to the $\omega_{12} = 0.331 (2\pi c/a)$ localized rod state. In this range, the real part of the dielectric function is qualitatively equivalent to the lossless case, and deviations never exceed 3.2%. Moreover, the TE band ending at ω_T inside the polariton gap closely follows the lowest TE band of the metallodielectric crystal, as in Fig. 16, which terminates at $0.458 (2\pi c/a)$. The PPC states can thus be chosen to lie well within the region of large negative dielectric and yet be sufficiently removed from ω_T to minimize the effects of losses.

Therefore, the node switching and flux expulsion phenomena can be realized with states subject to little perturbation due to their removal from ω_T by at least 2.5Γ . Key to this analysis involving LiTaO₃ are the large value of $\epsilon_0 = 13.4$ and the small ratio $\Gamma/\omega_T = 0.032$, and other materials with similar properties should also result in practical experimental utility. Indeed, we have verified these conclusions by explicitly including losses in select calculations for our model PPC system with LiTaO₃ rods.

VI. CONCLUSION

The ability to study many different optical response regimes using the same physical PPC structure is an extremely powerful tool. We have presented models for all of the relevant frequency domains of a polaritonic material: the high index region below ω_T , the metallic region above ω_T , and the low index region near ω_L . In previous works,^{12,13} the authors have noted the presence of flat, dispersionless bands

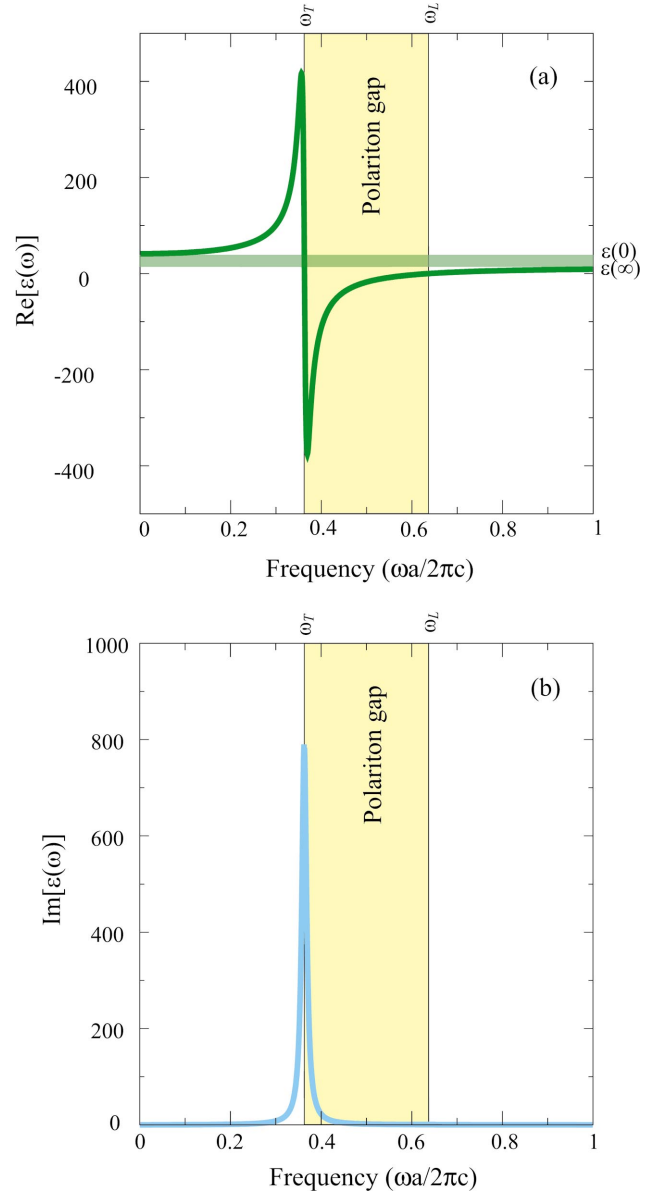


FIG. 19. (Color) The real and imaginary parts of the polariton dielectric function for LiTaO₃ with $\epsilon_\infty = 13.4$ and $a = 25.6 \mu\text{m}$, leading to normalized frequencies $\omega_T = 0.3628$, $\omega_L = 0.6372$, and $\Gamma = 0.0128$.

near ω_T . We verify these conclusions and provide a quantitative description for the origin of these bands related to the localized resonance modes of a high index slab (one dimension) or rod (two dimensions). The success of this model is shown to be excellent for a 1D slab PPC of CsI in air.

In a 2D square lattice of TiCl rods, a distinction between TE and TM polarizations is immediately apparent. Anticrossing behavior in the TE modes, contrasted against the flat TM bands reminiscent of the 1D PPC band structure, is explained by the interaction of the lowest metallodielectric TE band with the localized resonances of a single rod. We demonstrate that this conclusion is correct using a crystal of SiC rods with a larger value of ω_T inside the metallodielectric TE band gap to eliminate the anticrossing interactions. This property provides the unique opportunity to continuously

vary the coupling behavior of a TE band over a very small frequency range, since the nodal structure of the field inside the polariton rod matches different resonances of the isolated rod at Γ and at X.

A further use of the 2D metallodielectric band structure is to predict the presence of PPC bands directly above ω_T in the metallic regime. The locations of the TE and TM metallodielectric band gaps play the deciding role in determining if and where the PPC bands occur. By exploiting the adjacency of the large index and metallic regimes, it is possible to realize flux expulsion, effecting enormous changes in the location of the electromagnetic energy over a small frequency range.

In the region near ω_L , important points to note are the penetration of the phononlike band of the bulk polaritonic material near Γ into the polariton gap due to the air acting as a defect layer, inducing a nonzero wave vector at ω_L that we have determined analytically in one dimension. In addition, there is a characteristic frequency at which the crystal becomes transparent. We have calculated conditions under which this point is above or below the polariton gap.

For practical applications, the effects of losses in the polaritonic medium are at a maximum near ω_T . However, using LiTaO_3 as an example material, we found that the high index and metallic regimes overlap with frequency ranges in which the imaginary part of ϵ is relatively small. Therefore, all of these phenomena should be readily accessible experimentally.

We note that it is remarkable that we have been able to observe all of the above phenomena using a single geometric structure. For wave vectors between Γ and M, the continuous variation of the dielectric profile as a function of distance along the propagation direction introduces the need for a discretization approximation to the physical structure as well as a significant increase in computational resources. We have performed preliminary calculations to verify that our conclusions regarding the shape and position of the bands that lead

to the node switching and flux expulsion phenomena apply conceptually without any major modifications. The ability to vary the size of the rods and the translational symmetry group of the crystal should provide a further level of tunability to facilitate isolating many of the effects described in this work.

In addition, our research has provided compelling support for the inclusion of the vectorial eigenmode expansion method in the set of techniques such as layer Korrington-Kohn-Rostoker²² and the multiple multipole method,²³ suitable for not only polaritonic systems but any material with a frequency-dependent optical response. We have determined the eigenmode basis to be well converged at 40 for all frequency regimes of the PPC. In both accuracy and efficiency, this technique surpasses the traditional time-domain and plane-wave method techniques. It provides the means to tackle further problems involving polaritonic photonic crystals, including dissipative systems and more complicated crystal structures. Indeed, the complex wave-vector solutions for the eigenmode problem in the case of lossy materials are readily available, and only numerical problems related to the stability of the mode finder when losses are introduced have prevented a full band-structure calculation of a lossy PPC at this time. With further research, the nascent field of phonon-polariton excitations in photonic crystals promises to yield more exciting phenomena and developments.

ACKNOWLEDGMENTS

K. C. H. would like to thank Michelle Povinelli, Eleftherios Lidorikis, and Steven Johnson for many helpful discussions. Support for this research was provided by a Graduate Research Fellowship from the National Science Foundation and the MRSEC program of the NSF under Grant No. DMR-0213282. P. B. acknowledges support from the Flemish Fund for Scientific Research (FWO-Vlaanderen) for a postdoctoral fellowship.

*Electronic address: kch23@mit.edu

¹T.F. Crimmins, N.S. Stoyanov, and K.A. Nelson, *J. Chem. Phys.* **117**, 2882 (2002).

²J.A.S. Barker and R. Loudon, *Rev. Mod. Phys.* **44**, 18 (1972).

³E. Yablonovitch, *Phys. Rev. Lett.* **58**, 2059 (1987).

⁴S. John, *Phys. Rev. Lett.* **58**, 2486 (1987).

⁵J.D. Joannopoulos, R.D. Meade, and J.N. Winn, *Photonic Crystals: Molding the Flow of Light* (Princeton University, Princeton, NJ, 1995).

⁶S.G. Johnson, P.R. Villeneuve, S. Fan, and J.D. Joannopoulos, *Phys. Rev. B* **62**, 8212 (2000).

⁷Y. Fink, J.N. Winn, S. Fan, C. Chen, J. Michel, J.D. Joannopoulos, and E.L. Thomas, *Science* **282**, 1679 (1998).

⁸S. Fan, P.R. Villeneuve, J.D. Joannopoulos, M.J. Khan, C. Manolatou, and H.A. Haus, *Phys. Rev. B* **59**, 15 882 (1999).

⁹C. Kittel, *Introduction to Solid State Physics*, 7th ed. Wiley, New York, 1966).

¹⁰M. Sigalas, C.M. Soukoulis, E.N. Economou, C.T. Chan, and K.M. Ho, *Phys. Rev. B* **48**, 14 121 (1993).

¹¹M.M. Sigalas, C.M. Soukoulis, C.T. Chan, and K.M. Ho, *Phys. Rev. B* **49**, 11 080 (1994).

¹²W. Zhang, A. Hu, X. Lei, N. Xu, and N. Ming, *Phys. Rev. B* **54**, 10 280 (1996).

¹³V. Kuzmiak, A.A. Maradudin, and A.R. McGurn, *Phys. Rev. B* **55**, 4298 (1997).

¹⁴A.Y. Sivachenko, M.E. Raikh, and Z.V. Vardeny, *Phys. Rev. A* **64**, 013809 (2001).

¹⁵N. Eradat, A.Y. Sivachenko, M.E. Raikh, and Z.V. Vardeny, *Appl. Phys. Lett.* **80**, 3491 (2002).

¹⁶P. Bienstman and R. Baets, *Opt. Quantum Electron.* **33**, 327 (2001).

¹⁷E. McRae, *Surf. Sci.* **11**, 479 (1968).

¹⁸N.A. Nicorovici, A.A. Asatryan, L.C. Botten, K. Busch, R.C. McPhedran, C.M. de Sterke, P.A. Robinson, G.H. Smith, D.R. McKenzie, and A.R. Parker, in *Conference on Photonic Crystals and Light Localization in the 21st century*, Vol. 563 of *NATO Science Series C: Mathematical and Physical Sciences*, edited by C. M. Soukoulis (Kluwer, Dordrecht 2001).

¹⁹V. Kuzmiak, A.A. Maradudin, and F. Pincemin, *Phys. Rev. B* **50**, 16 835 (1994).

²⁰E. Lidorikis, M.M. Sigalas, E.N. Economou, and C.M. Soukoulis, Phys. Rev. Lett. **81**, 1405 (1998).

²¹M. Schall, H. Helm, and S.R. Keiding, Int. J. Infrared Millim. Waves **20**, 595 (1999).

²²A. Modinos, N. Stefanou, and V. Yannopapas, Opt. Express **8**, 197 (2001).

²³E. Moreno, D. Erni, and C. Hafner, Phys. Rev. B **65**, 155120 (2002).